

# PROCEEDINGS OF SPIE

[SPIDigitalLibrary.org/conference-proceedings-of-spie](https://SPIDigitalLibrary.org/conference-proceedings-of-spie)

## Numerical modeling of a dark current suppression mechanism in IR detector arrays

Glasmann, Andreu, Hubbard, Taylor, Bellotti, Enrico

Andreu Glasmann, Taylor Hubbard, Enrico Bellotti, "Numerical modeling of a dark current suppression mechanism in IR detector arrays," Proc. SPIE 10177, Infrared Technology and Applications XLIII, 101770A (16 May 2017); doi: 10.1117/12.2265901

**SPIE.**

Event: SPIE Defense + Security, 2017, Anaheim, California, United States

# Numerical Modeling of a Dark Current Suppression Mechanism in IR Detector Arrays

Andreu Glasmann, Taylor Hubbard, and Enrico Bellotti\*

Boston University, Department of Electrical and Computer Engineering, 8 St. Mary's St.,  
Boston, MA 02215;

## ABSTRACT

As material growth and processing have improved, state of the art infrared detector arrays remain limited by material properties and not processing or growth quality. In particular, the dark current can be dominated by diffusion of minority carriers in the quasineutral regions. In this work, we present a unique detector architecture that allows for dark current suppression below the fundamental diffusion limit. We have extensively studied this effect, and report dark current, photocurrent, and quantum efficiency. Finally, we conclude by offering a path to implementing this architecture into existing FPAs.

**Keywords:** short wavelength infrared, SWIR, InGaAs, FPA, numerical modeling, dark current, infrared photodetectors, dark current suppression

## 1. INTRODUCTION

Dark current is arguably one of the most commonly used parameters to judge and compare infrared detector performance. Understanding, predicting, and optimizing this parameter is critical to engineer these detectors for applications in astronomy, night vision, target identification, and research. Outside of background limited detectors, such as those used for MWIR and LWIR detection, dark current sets the limit on minimum detectable light level; if the dark current is too large, it will mask the photocurrent created by incident radiation. Here, we present an architecture that can effectively control and suppress a component of dark current in infrared detector arrays. Using 1D analytical expressions for minority carriers, we introduce the underlying theory. Then, using a 3D drift-diffusion model, we show that this can be used to lower the dark current in SWIR InGaAs detectors. Finally, we conclude with discussing the benefits and drawbacks of this method.

Third generation infrared detectors are commonly fabricated using either planar or mesa formats which are subsequently hybridized to a silicon read-out circuit. Mesa structures can be advantageous due to purely vertical carrier transport, resulting in no lateral diffusion current and reduced optical crosstalk [1]. However, poorly passivated surfaces can lead to leaky devices since the junction extends to the mesa edge, allowing carrier generation through surface states [2, 3]. Planar devices simplify fabrication, can achieve smaller pixel sizes, and may offer superior dark current performance at the cost of increased crosstalk. In this work, we discuss a way of suppressing the lateral diffusion current in planar detectors. Unless otherwise specified, we are discussing lattice-matched  $\text{In}_{0.53}\text{Ga}_{0.47}\text{As}$  photodetectors using a planar  $p^+n$  format. The theory and methodology shown here can be readily applied to other material systems and detector architectures.

The manuscript is organized as follows: Section 2 introduces the basic concepts that we exploit to suppress the dark current, and Section 3 discusses our numerical model and simulation methodology. Section 4 presents the results and Section 5 concludes the article by offering a path to successful FPA implementation.

---

\*email bellotti@bu.edu; phone (617) 358-1576

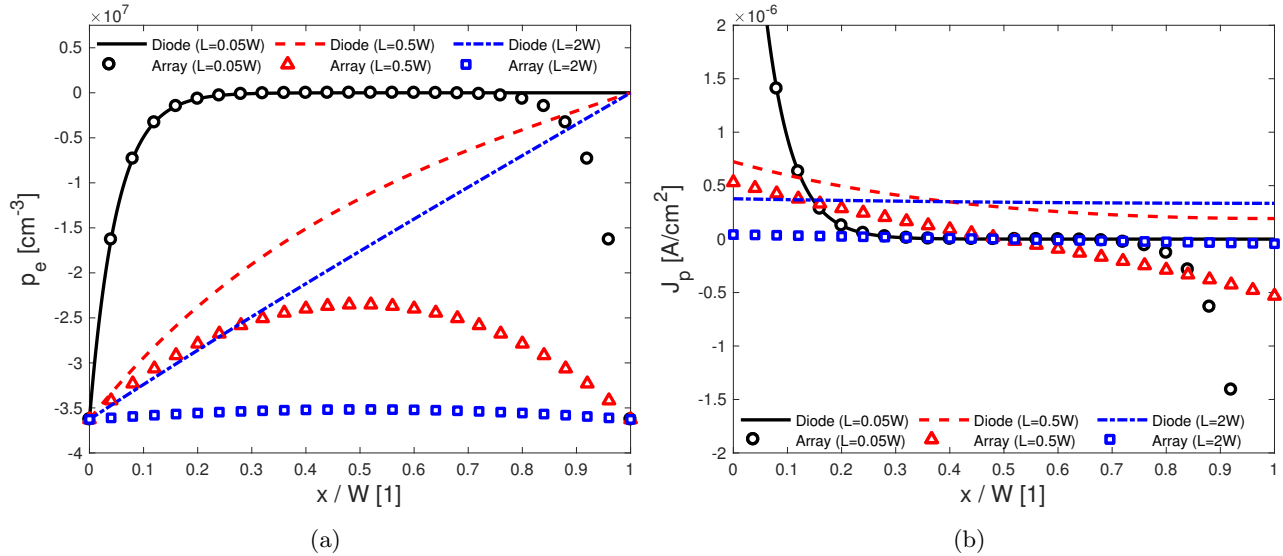


Figure 1: Analytically computed curves for the (a) minority carrier concentration and (b) current densities as functions of normalized position using diode and array boundary conditions. Material parameters are based on  $\text{In}_{0.53}\text{Ga}_{0.47}\text{As}$ ,  $T = 300\text{K}$ ,  $N_d = 10^{16}\text{cm}^{-3}$ , and  $V_1 = V_2 = -0.1\text{V}$ .

## 2. THEORY

State of the art SWIR  $\text{In}_{0.53}\text{Ga}_{0.47}\text{As}$  and MW/LWIR  $\text{HgCdTe}$  arrays are typically limited by intrinsic recombination mechanisms which permit full-gap transitions of carriers. Consequently, these materials are often limited by radiative or Auger recombination in the quasi-neutral regions. The net recombination rate determines the shape of the minority carrier profile on each side of the junction. In the case of a  $p^+n$ -junction, with a shallow  $p^+$  diffusion, we will only consider holes in the quasi-neutral  $n$ -side, but this analysis still holds for the opposite polarity. Outside of the depleted region, the continuity equation for holes simplifies to [4]

$$\frac{\partial p_e}{\partial t} = D_p \nabla^2 p_e - \frac{p_e}{\tau_p}, \quad (1)$$

where we have assumed low injection to simplify the generation/recombination term, a position independent diffusivity, and used the fact the  $p = p_{n0} + p_e$ , where  $p$ ,  $p_{n0}$ , and  $p_e$  are the values for the minority carrier concentration, equilibrium hole concentration on the  $n$ -side, and the excess carrier concentration respectively. Once we assume steady-state, the partial derivative on the left-hand side with respect to time vanishes, and we are left with a second order homogeneous differential equation. In order to obtain an expression for the hole concentration, we need to apply two appropriate boundary conditions. We will look at two separate cases in 1D that impose different boundary conditions: (1) a single diode — used as model validation and a baseline to compare with — and (2) two neighboring diodes — reflecting the applicable boundary condition in detector arrays.

### 2.1 Single Diode Solution

A standalone diode solution is achieved by applying boundary conditions at the depleted region edge on the  $n$ -side (defined as  $x = 0$ ) and at the metal contact on the other edge (defined as  $x = W_n$ ). For the depleted edge at  $x = 0$ , the excess hole concentration is controlled by the bias applied to the junction  $p_e(x = 0) = p_{n0} [\exp(qV_1/kT) - 1]$ . Note the three limiting cases: for  $V_1 \rightarrow +\infty$ ,  $p_e(x = 0) = +\infty$ ;  $V_1 \rightarrow 0$ ,  $p_e(x = 0) = 0$ , and  $V_1 \rightarrow -\infty$ ,  $p_e(x = 0) = -p_{n0}$ . Hence, when reverse biased beyond a few  $kT/q$ , the boundary condition quickly converges to a constant value. On the other side at  $x = W_n$ , we can assume that there is a perfect ohmic contact (negligible surface recombination) that holds the minority carrier concentration at the equilibrium value such that  $p_e(x = W_n) = 0$ . The results of these boundary conditions are shown as lines in Fig. 1. This simple example is what is often referred to as “long” and “short” base diode expressions — to illustrate this, we have also plotted

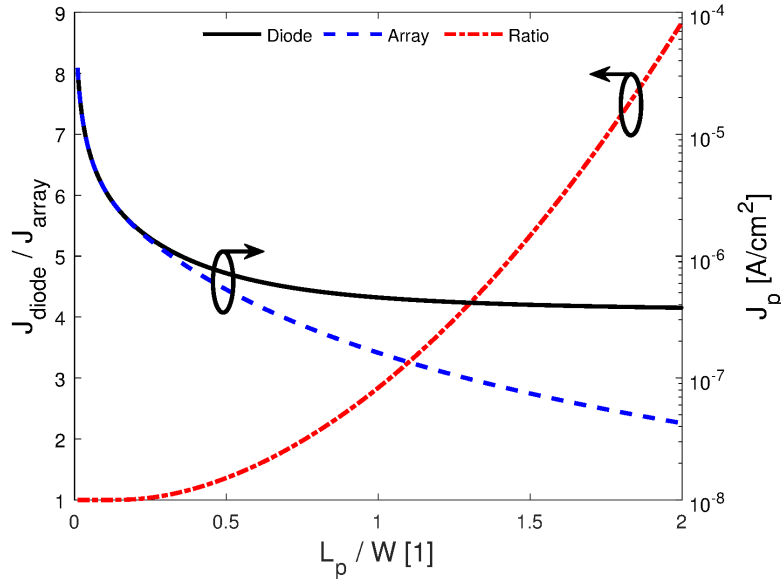


Figure 2: Analytically calculated current density at  $x = 0$  is plotted on the right y-axis for a standalone diode and two neighboring diodes as a function of minority carrier diffusion length. The ratio of the two currents is plotted on the left axis. Once  $L_p \approx 0.5W_n$ , the current measured by diodes in an array begins to be suppressed. Material parameters are based on  $\text{In}_{0.53}\text{Ga}_{0.47}\text{As}$ ,  $T = 300\text{K}$ ,  $N_d = 10^{16}\text{cm}^{-3}$ , and  $V_1 = V_2 = -0.1\text{V}$ .

each curve as a function of minority carrier diffusion length. In the limit that  $L_p \ll W_n$  (shown as  $L_p = 0.05W_n$ ), we observe that the minority carrier profile quickly returns to the equilibrium value. Furthermore, this also gives the largest value of dark current shown in Fig. 1(a). Second, in the case that  $L_p \gg W_n$  (shown as  $L_p = 2W_n$ ), we have the short base diode as expected — the minority carrier profile is linear, and gives the smallest value of dark current. This case is evidence that our analytical model is able to recover the anticipated minority carrier characteristics.

## 2.2 Neighboring Diodes Solution

In previous work, Wichman et al. showed in Ref. 5 that the typical  $pn$ -junction boundary conditions outlined in Section 2.1 do not hold when considering an array of diodes where the minority carrier diffusion length is equal to or greater than the pixel pitch. In particular, they noted that there are symmetry planes in an array where the lateral diffusion current between pixels is zero. Therefore, an appropriate boundary condition for their conclusion is that  $J_p(x = W_n/2) = 0$ , where  $W_n$  in this case is the array's pixel pitch and  $J_p$  is the current density. This, however, only holds for the specialized case where all the diodes in the array are held at the same bias. Here, we present a more generalized solution by instead considering the boundary conditions at each pixel's depleted region edge, or a  $pn$  device. Now, the two boundary conditions are  $p_e(x = 0) = p_{n0} [\exp(qV_1/kT) - 1]$  and  $p_e(x = W_n) = p_{n0} [\exp(qV_2/kT) - 1]$ , where  $W_n$  represents the distance between the depletion region edges of neighboring junctions,  $V_1$  and  $V_2$  are the voltages applied to each junction.

Figure 1 also shows the results of this change of boundary condition for different minority carrier diffusion lengths. We see that when  $V_1 = V_2$ , we are able to successfully reproduce the findings of Ref. 5. At  $x/W = 0.5$ , or halfway between neighboring diodes, we see that the minority carrier concentration reaches a maximum value in Fig. 1(a) and the current density goes to zero in Fig. 1(b). Practically, this symmetry point can be thought of as the boundary between the active regions of the two neighboring pixels — carriers located at  $x/W < 0.5$  will be extracted at the contact on that side, and carriers located at  $x/W > 0.5$  will be extracted by the other contact. This result is also reflected in the signs of the current densities in Fig. 1(b). At  $x/W = 0$  and  $x/W = 1$  the current density observed at the contacts are equal in magnitude and opposite in sign, representing carriers flowing in opposite directions.

Figure 2 shows how the dark current changes with this new boundary condition by plotting the dark current as a function of normalized diffusion length. Once  $L_p \approx 0.5W$ , the dark current sensed by a diode in an array becomes suppressed relative to single diode. As the diffusion length increases — or equivalently, as the inter-diode spacing is reduced — the degree of dark current suppression increases. At  $L_p \approx 2W$ , the pixel dark current in an array is nearly an order of magnitude smaller.

### 2.3 Diffusion Control Junctions

The previous section describes the underlying physics that we are exploiting to control dark current in IR detector arrays. Instead of viewing the two junctions as neighboring pixels, consider using the second junction as an additional parameter to control the dark current. Since this phenomenon relies on modifying the diffusion characteristics of the pixel, we will refer to this extra diffused region as a “diffusion control junction” (DCJ), and the original junction as the “sensing junction” (SJ).

### 2.4 Extension to 3D

We have analyzed the 1D characteristics of what is essentially a *pn* or *pn**p* device. The basic dependencies of the minority carrier expressions remain when moving into a higher dimension, but manifests with different geometrical coefficients[6], and ultimately fails to be explained by the 1D case. Most important to understanding this effect is the distinction between *lateral* and *vertical* transport. Consider a set of cylindrical diffusions forming a diode array. Vertically, each junction behaves like the normal *pn*-junction presented in Section 2.1\*. In the quasineutral region between junctions, the solution behaves like the *pn**p* device shown in Section 2.2. In order to realize the dark current suppression, the detector array needs to be dominated by the *lateral* contribution to the dark current. Fortunately, SWIR  $\text{In}_{0.53}\text{Ga}_{0.47}\text{As}$  is an ideal material system to study this effect — the planar DLPH structure is dominated by lateral diffusion, and the minority carrier diffusion length is longer than the pixel dimensions. Finally, it is important to note that the pixel geometry plays an important role in determining whether or not the diode is dominated by lateral diffusion current. If the diffused junction radius is too small or too large, the vertical contribution can dominate. For this work, we have chosen a junction radius of  $2\text{ }\mu\text{m}$  on a  $15\text{ }\mu\text{m}$  to  $20\text{ }\mu\text{m}$  pixel pitch.

## 3. 3D NUMERICAL SIMULATIONS

In order to predict device performance, we employ a three dimensional finite element drift-diffusion model to simultaneously solve Poisson’s equation coupled with electron and hole continuity equations. In the absence of any optical generation, this process yields the dark current characteristics as a function of applied bias and temperature. In order to simulate the optical generation in the device, we use a finite-difference time-domain approach on a tensor grid. This optical generation result is then interpolated onto a finite-element mesh for further device simulation. Hence, we are able to calculate device-level measurables, including quantum efficiency (QE), dark current, and photocurrent.

Shown in Fig. 3(a) is an example of the structure used to perform the simulations. The epitaxial layer thicknesses, doping densities, and geometry are chosen to replicate the typical architecture used in SWIR  $\text{In}_{0.53}\text{Ga}_{0.47}\text{As}$  detectors:  $2\text{ }\mu\text{m}$   $N^+$ -InP substrate  $N_d = 2 \times 10^{18}\text{ cm}^{-3}$ ,  $0.5\text{ }\mu\text{m}$   $N^+$ -InP buffer  $N_d = 2 \times 10^{18}\text{ cm}^{-3}$ ,  $3\text{ }\mu\text{m}$   $n$ - $\text{In}_{0.53}\text{Ga}_{0.47}\text{As}$  absorber  $N_d = 10^{16}\text{ cm}^{-3}$ , and  $0.5\text{ }\mu\text{m}$   $N$ -InP cap  $N_d = 10^{16}\text{ cm}^{-3}$ . We assume abrupt cylindrical diffusion that persists to  $200\text{ nm}$  into the  $\text{In}_{0.53}\text{Ga}_{0.47}\text{As}$  absorber with  $N_a = 10^{18}\text{ cm}^{-3}$ , forming a  $P^+-p^+-n-N^+$  DLPH detector.

---

\*Notice, however, that the vertical boundary condition does not necessarily need to be the perfect ohmic contact shown here. A more appropriate boundary condition for a DLPH detector would be that  $J_p(x = W_n) = 0$ , as the  $N^+$  substrate reflects all holes away from the cathode.

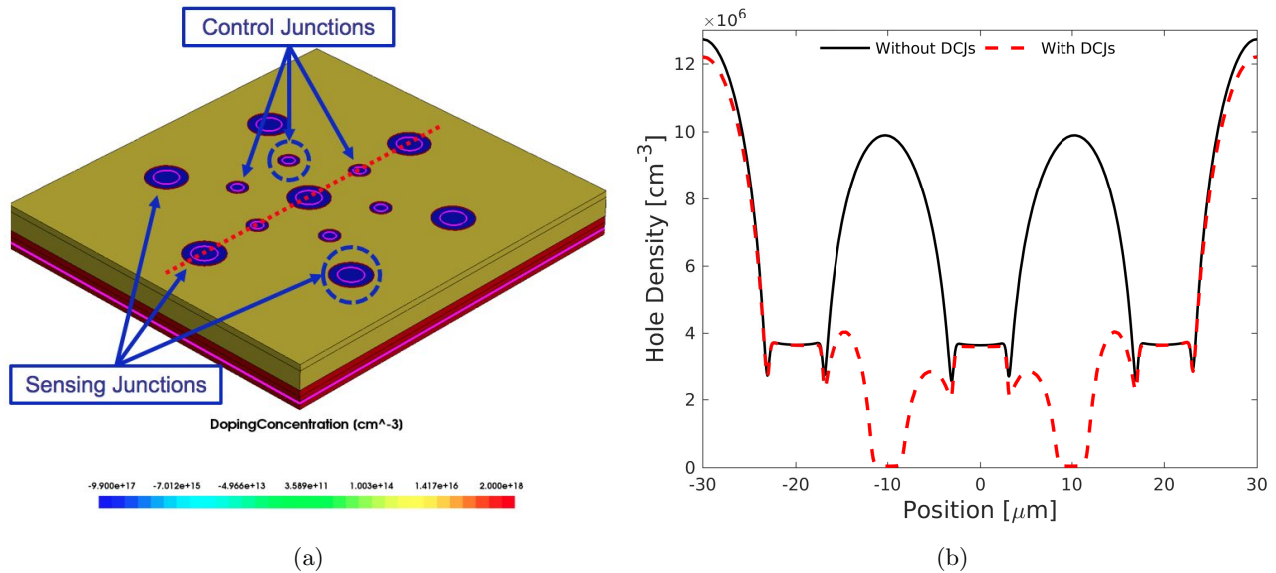


Figure 3: (a) A finite-element mesh used to simulate the performance of a 20  $\mu\text{m}$  pitch hexagonal  $\text{In}_{0.53}\text{Ga}_{0.47}\text{As}$  array. The larger circles are the sensing junctions and the smaller circles are the control junctions. (b) Numerically computed hole density between the junction formed in the absorber along the dashed line shown in (a). The control junctions are placed at  $\pm 10 \mu\text{m}$ .

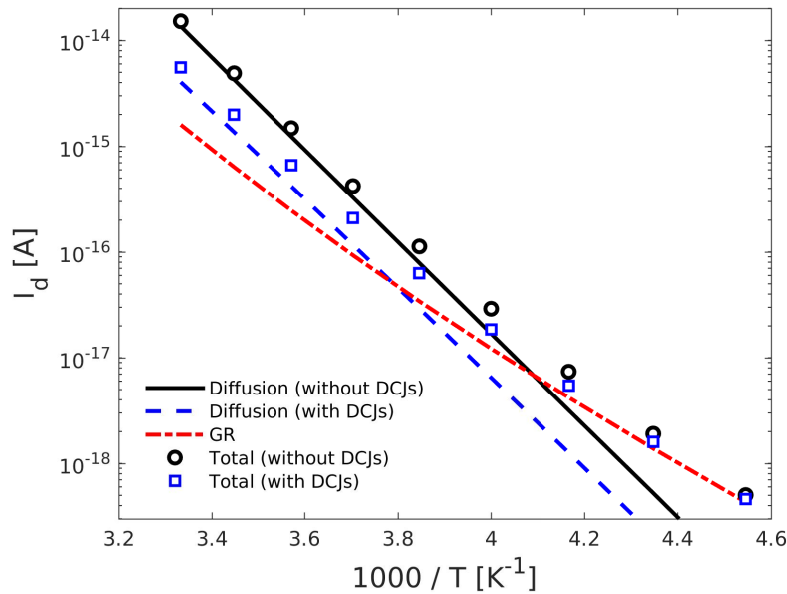


Figure 4: Numerically computed arrhenius plot of the dark current for temperatures between 220 K and 300 K using the geometry shown in Fig. 3.  $V_{SD} = -0.1 \text{ V}$ ,  $V_{DCJ} = -0.2 \text{ V}$ ,  $\tau_{\text{SRH}} = 107 \mu\text{s}$ .

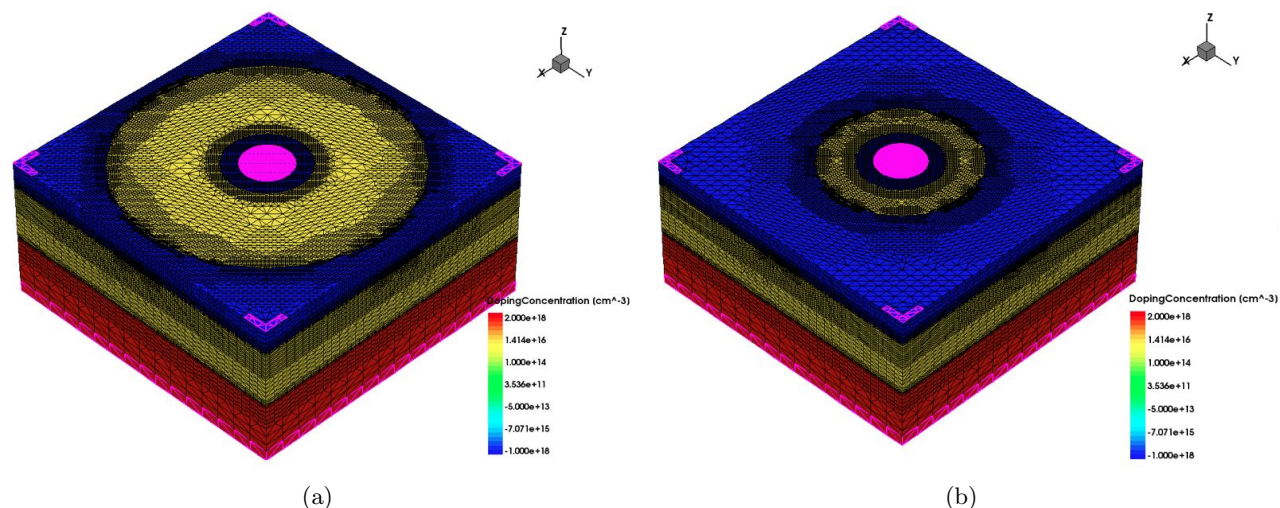


Figure 5: Pixels with DCJ structures that improve the lateral dark current suppression. The two structures are identical other than the spacing between the SJ and DCJ, and have the same epitaxial stack as Fig. 3. The spacings between the SJ and DCJ are  $4.75\ \mu\text{m}$  and  $1.75\ \mu\text{m}$  for (a) and (b) respectively.

## 4. RESULTS

### 4.1 1D Validation

Figure 3 gives an example of one possible DCJ implementation. The control junctions are placed at the pixel boundaries in the hexagonal  $\text{In}_{0.53}\text{Ga}_{0.47}\text{As}$  array shown in 3(a). In this case, the sensing diodes are held at  $-0.1\ \text{V}$  and the control diodes are at  $-0.2\ \text{V}$ . Since the reverse bias is small, there is a noticeable change in the boundary condition at the depleted region edge of the control junctions when compared to the sensing junctions, seen in Fig. 3(b). This unoptimized example shows that the additional junctions modulate the minority carrier profile in a similar way to the 1D analytical model presented earlier.

Figure 4 shows the device simulation results for the geometry presented in Fig. 3. When the detector is diffusion limited at high temperatures, the DCJs are actively suppressing the dark current measured at the center diode. Since the SRH GR current is dependent on the geometry of the depleted region and is independent of the diffusion current, the DCJ effect is negligible. Hence, material systems that are GR-limited will not see the benefit of DCJ implementation. For this geometry we observe approximately  $5\times$  reduction in dark current. The GR current was calculated by subtracting the total current, which includes SRH, Auger, and radiative mechanisms, from the diffusion current which only includes Auger and radiative.

### 4.2 Improved Dark Current Suppression and QE Loss

In order to understand the influence of control junction geometry on the dark current reduction, we generated the structures shown in Fig. 5. By diffusing an outer control junction ring, we exploit radial symmetry to improve the suppression of the minority carrier profile. In order to assess the optical performance of the device, we consider three cases: (1) a standard pixel without DCJs, uniformly illuminated; (2) a pixel with the new DCJ geometry, uniformly illuminated; and (3) a pixel with the DCJ geometries, but with a microlens focusing the incident light from an uniform illumination onto the sensing junction. We report the results in terms of a photo to dark current ratio and quantum efficiency. The ratio is important to understand how the dark current changes the sensitivity of the device, while the QE is important to determine the amount of photogenerated carriers that are lost to the DCJs.

The photo to dark current ratios are shown in Fig. 6. For the case with a larger SJ-DCJ spacing, the benefit of DCJ implementation is small. In Fig. 6(a), there is a small improvement in the photo to dark current ratio of  $2\times$ . The cause of the minimal improvement is due to lost photocurrent to the DCJs which is reflected in the QE plotted in 7. Finally, it is worth noting that similar to what was shown in Fig. 3, the DCJ is not effective



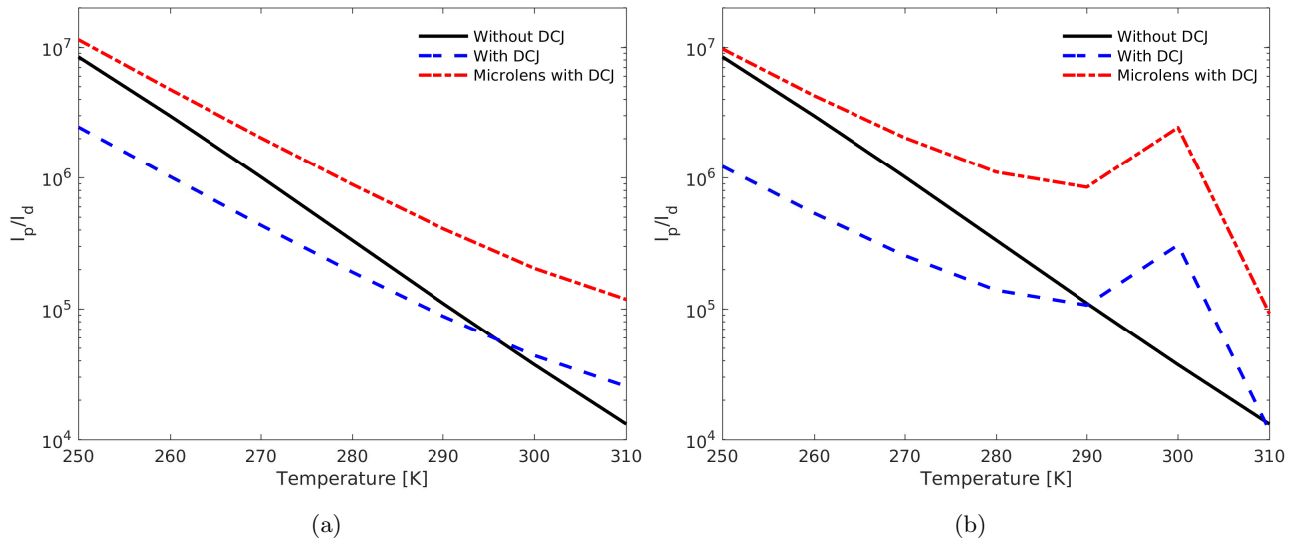


Figure 6: Photo to dark current ratios plotted as a function of temperature for the geometries shown in Fig. 5. The photon flux and wavelength are chosen to be  $10^{14}$  photons  $\text{s}^{-1} \text{cm}^{-2}$  and  $1.5 \mu\text{m}$ .

at low temperatures due to the device being GR limited, and performance is degraded. In the following section we discuss a viable mitigation strategy.

Now consider the geometry with reduced spacing between the SJ and DCJ. The ratios shown in 6(b) show significant improvement over the previous case. Now, at 300K we observe an order of magnitude improvement in the photo to dark current ratio. However, the smaller spacing also further lowers the QE of the device. Finally, we need to address the discontinuity near 300K. This is a direct consequence of how we are modulating the minority carrier profile. For temperatures larger than 300K, the slope of the minority carrier profile at the sensing junction has changed sign. This means that the sensing diode is now sourcing carriers that are extracted by the control junction, effectively preventing photodetector operation. True optimization of the DCJ-SJ spacing lies somewhere between the two cases presented here.

### 4.3 QE Recovery Using Microlenses

Figures 6 and 7 also show the DCJ performance when coupled with microlenses. The work presented here is unoptimized, and only shown for one particular lens geometry. For the results shown here, the microlens shows substantial improvement over the standard DCJ implementation. The lower temperature operation of the device is recovered, the QE is still lower than the baseline diode, but is 40% higher than the previous cases, and the photo to dark current ratio at 300K is now about an order of magnitude for the largest spacing, and two orders of magnitude for the smallest spacing. Finally, the peak at  $1 \mu\text{m}$  in the QE graphs is likely from chromatic aberration of the lens. More work is required to optimize the QE for the SWIR band.

## 5. CONCLUSION

If the detector fabrication tolerances do not allow for small-format arrays, the DCJ approach provides a way to improve device performance at the cost of wafer fill factor. In order to avoid hybridizing each additional junction, and modifying the existing ROIC, we suggest using rows and columns of highly-doped areas to control the diffusion current. With this approach, only an additional contact for DCJ biasing is required.

In this work, we have used our numerical model to study a way to reduce the dark current in  $\text{In}_{0.53}\text{Ga}_{0.47}\text{As}$  detector arrays. By placing additional junctions in the 2D array, it is possible to achieve small-format performance with existing fabrication processes. The major disadvantage of implementation is the loss of photocurrent, and consequently, quantum efficiency. There is numerical evidence that coupling the additional junctions with microlens arrays will recover the lost quantum efficiency, while maintaining the dark current reduction. This technology is particularly well suited for low-light level applications where the dark current is greater than the



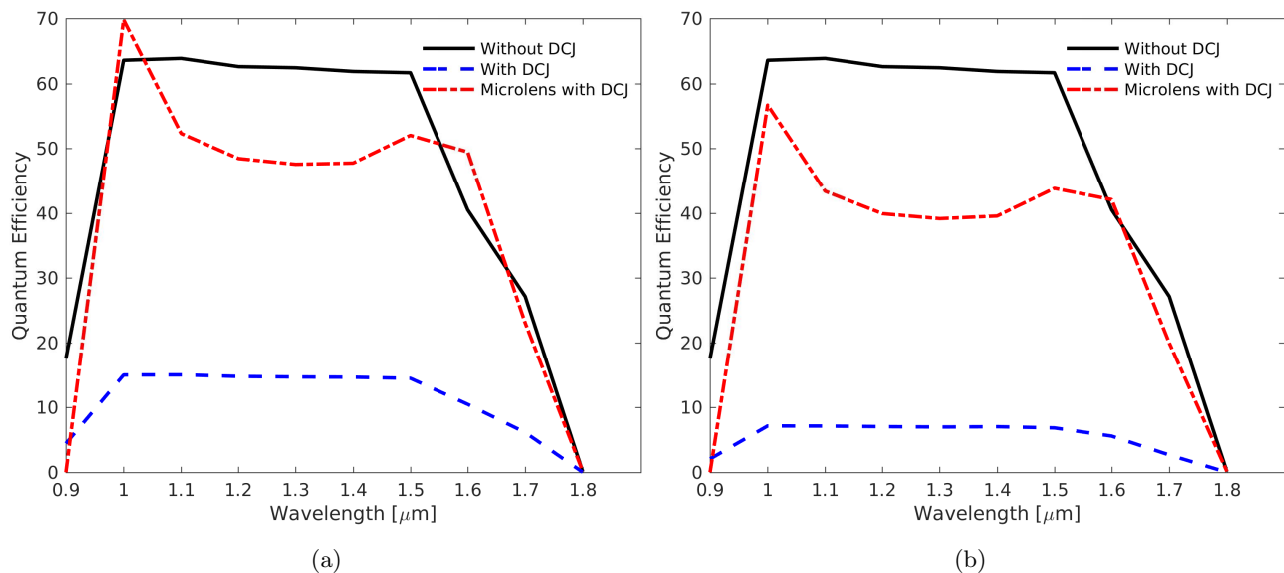


Figure 7: Quantum efficiency plotted as a function of wavelength for the geometries shown in Fig. 5. The incident photon flux is  $10^{14}$  photons  $\text{s}^{-1} \text{cm}^{-2}$ . Please note that we are not accounting for any reflection off of the InP substrate—which has been evaluated to be near 30%.

generated photocurrent; by implementing the DCJs, we can reduce the dark current and recover an image. The net benefit in introducing the extra junctions can be assessed by considering the lateral and vertical boundary conditions imposed by the detector architecture.

## ACKNOWLEDGMENTS

The authors would like to credit and thank Mr. Adam Wichman for the discovery and preliminary work in simulating this effect. Furthermore, the authors would also like to thank Dr. Benjamin Pinkie, Dr. Jonathan Schuster, Dr. Wijewarnasuriya Priyalal, and Dr. Marion Reine for useful discussions and guidance. This work was generously funded by the DARPA MTO.

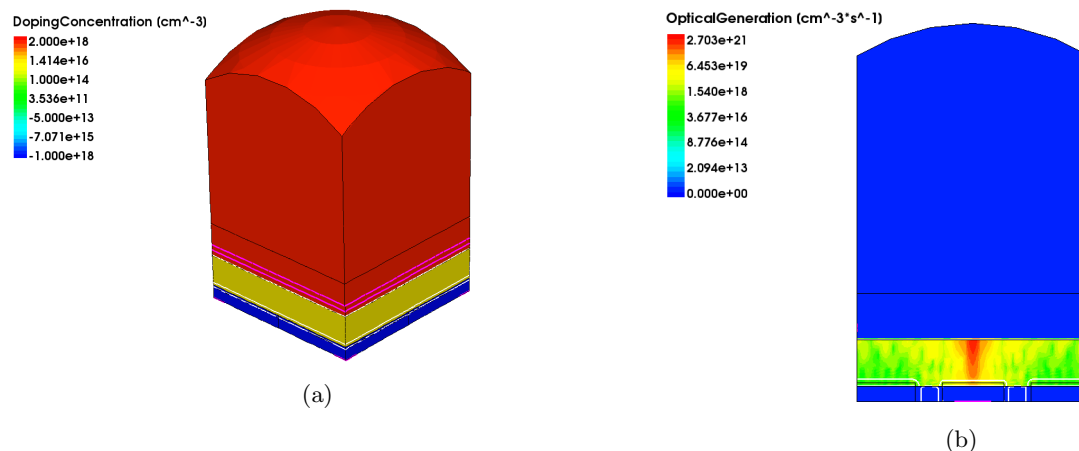


Figure 8: An example of the microlens structure used to perform the optical simulations. On the left is the 3D finite element mesh with the microlens etched onto the back of the InP substrate. The right shows the optical generation profile, revealing successful focusing of the incident radiation.

## APPENDIX A. In<sub>0.53</sub>Ga<sub>0.47</sub>As MATERIAL PARAMETERS

Table 1: In<sub>0.53</sub>Ga<sub>0.47</sub>As parameters reproduced from Ref. 7.

Parameter Name	Model	Units	Reference
Bandgap	$E_g(T) = 0.731 - 3.34 \times 10^{-4}(T - 300)$	eV	[8]
Effective Masses	$m_n^*/m_0 = 0.041$ $m_{hh}^*/m_0 = 0.46$	1	[9]
Absorption Coefficient	Data from Ref.	cm <sup>-1</sup>	[8, 10]
Radiative Recombination	$\tau^{rad} = 1/N_d B(T)$	s	[11]
	$B(T) = 9.5 \times 10^{-11}(T/300)^{-1.68}$	cm <sup>3</sup> /s	
Auger Recombination	$\tau^{Aug} = 1/N_d^2 C$	s	[11]
	$C = 8.1 \times 10^{-29}$	cm <sup>6</sup> /s	
SRH Recombination	$\tau^{SRH} = 107 \times 10^{-6}$	s	[12]
	$E_t = E_i$	eV	
Mobilities	$\mu_e = 1.24 \times 10^4 (T/300)^{-1.405}$	cm <sup>2</sup> / Vs	[13]
	$\mu_p = 234 (T/300)^{-1.42}$		

## References

- [1] Pinkie, B. and Bellotti, E., “Numerical simulation of the modulation transfer function in HgCdTe detector arrays,” *Journal of electronic materials* **43**(8), 2864 (2014).
- [2] Rutkowski, J., “Planar junction formation in HgCdTe infrared detectors,” *Opto-Electronics Review* **12**(1), 123–128 (2004).
- [3] Arias, J., Pasko, J., Zandian, M., Shin, S., Williams, G., Bubulac, L., DeWames, R., and Tennant, W., “Planar p-on-n HgCdTe heterostructure photovoltaic detectors,” *Applied physics letters* **62**(9), 976–978 (1993).
- [4] Muller, R. and Kamins, T., [*Device Electronics for Integrated Circuits*], John Wiley and Sons (2003).
- [5] Wichman, A., Pinkie, B., and Bellotti, E., “Dense array effects in SWIR HgCdTe photodetecting arrays,” *Journal of Electronic Materials* **44**(9), 3134–3143 (2015).
- [6] Grimbergen, C., “The influence of geometry on the interpretation of the current in epitaxial diodes,” *Solid-State Electronics* **19**(12), 1033–1037 (1976).
- [7] Wichman, A. R., DeWames, R. E., and Bellotti, E., “Three-dimensional numerical simulation of planar P+n heterojunction In<sub>0.53</sub>Ga<sub>0.47</sub>As photodiodes in dense arrays part I: Dark current dependence on device geometry,” in [*SPIE Defense+ Security*], 907003–907003, International Society for Optics and Photonics (2014).
- [8] Zielinski, E., Schweizer, H., Streubel, K., Eisele, H., and Weimann, G., “Excitonic transitions and exciton damping processes in InGaAs/InP,” *Journal of applied physics* **59**(6), 2196–2204 (1986).
- [9] Adachi, S., [*Physical properties of III-V semiconductor compounds*], John Wiley & Sons (1992).
- [10] Munoz, M., Holden, T. M., Pollak, F. H., Kahn, M., Ritter, D., Kronik, L., and Cohen, G. M., “Optical constants of In<sub>0.53</sub>Ga<sub>0.47</sub>As/InP: experiment and modeling,” *Journal of applied physics* **92**(10), 5878–5885 (2002).

- [11] Ahrenkiel, R., Ellingson, R., Johnston, S., and Wanlass, M., "Recombination lifetime of In<sub>0.53</sub>Ga<sub>0.47</sub>As as a function of doping density," *Applied Physics Letters* **72**(26), 3470–3472 (1998).
- [12] DeWames, R., Littleton, R., Witte, K., Wichman, A., Bellotti, E., and Pellegrino, J., "Electro-optical characteristics of P+ n In<sub>0.53</sub>Ga<sub>0.47</sub>As hetero-junction photodiodes in large format dense focal plane arrays," *Journal of Electronic Materials* **44**(8), 2813–2822 (2015).
- [13] Madelung, O., [*Semiconductors: Group IV elements and III-V compounds*], Springer Science & Business Media (2012).